Design and Demonstration of a Lattice-Based Target for Hyperspectral Subpixel Target Detection Experiments

Chase Cañas, *Graduate Student Member, IEEE*, and John P. Kerekes, *Senior Member, IEEE*

***Abstract*— A lattice-based target design is presented for expanding research capabilities in subpixel target detection. The targets generate large numbers of subpixel samples with a priori knowledge of the exact subpixel fractions. This contrasts with traditional targets, where subpixel fractions are either unknown or estimated with significant uncertainty, with limited samples available in historical datasets. The subpixel targets diminish these drawbacks and generate constant subpixel samples invariant to effects of the system (e.g., image distortions, scan pattern) which would typically induce uncertainty. Simulations were performed to assess the accuracy of the proposed method of achieving samples with constant fractions. To validate and demonstrate the functionality of the design, four targets were fabricated with constant subpixel fractions (0.2, 0.4, 0.6, 0.8) and were deployed into a hyperspectral data collection. Spectral unmixing validated the retrieval of samples with constant fractions, and a general target detection scenario was demonstrated using 300–400 samples of each constant fraction. The impacts of a limited number of target samples (e.g., $n = 5, 10$) on receiver operating characteristic (ROC) curves were empirically assessed, with a significant reduction of variability observed when $n > 100$, illustrating the advantages when large sample sizes are available. Design limitations are discussed, along with applications (e.g., algorithm comparison) for the community.**

***Index Terms*— Algorithm comparison, fill fraction, ground truth, object detection, remote sensing, spectral unmixing.**

I. Introduction

DETECTION of subpixel targets is achievable with hyperspectral technology and proven image processing algorithms [1], [2], [3], [4]. In historical datasets, subpixel fractions of target samples are unknown with exact precision, given the remote sensing system induces various distortions due to the optical response, scan pattern, and image processing errors. Subpixel targets are also difficult to manually label (i.e., ground truth mask) given uncertainty associated whether mixed pixels are actually targets or background. As a result, historical datasets for subpixel detection typically consist of a limited number of subpixel samples [5], which implies performance evaluations are inconclusive for determining absolute algorithm superiority [6]. To resolve these issues, a novel target design is proposed and demonstrated for expanding research in subpixel detection.

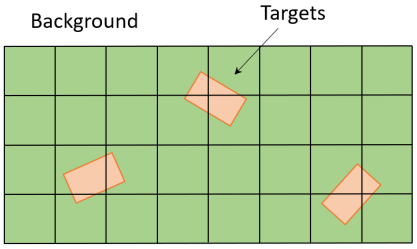

Fig. 1. Random phasing of traditional targets across the projection of image pixels onto the ground.

Hyperspectral imaging (HSI) sensors measure spectra of radiant energy segmented across dozens, hundreds, or even thousands of spectral bands. In remote sensing, HSI cubes consist of spectral and spatial dimensions which are processed with algorithms to automate the detection of rare objects in the scene. Although spatially unresolved, subpixel targets are detectable through the exploitation of a material's spectral features.

Traditional targets are observable across a variety of target detection datasets [7], [8], [9], [10], [11], [12]. Depending on the size of the target relative to the ground sample distance (GSD) of the sensor, subpixel samples will either reside across edges or central regions of the target. A primary issue when establishing ground truth information of the subpixel fraction is the random phasing (or placement) of the targets across the projection of the image pixels onto the ground [13]. This is visualized in Fig. 1, where the scan pattern from the sensor determines the partition of the target and background material within the projection of pixels onto the ground. An overall list of issues associated with traditional targets include the following.

1) *Pixel Phasing:* Random phasing (i.e., orientation) of the target across the image pixels.
2) *Sample Size:* Small number of target samples implies large confidence intervals in empirical receiver operating characteristic (ROC) curves.
3) *Image Blur:* The point spread function (PSF) of the sensor blurs the target and background objects.
4) *Geometric Processing:* Geo-referencing errors distort the true mapping between object and image space.

Manuscript received 30 March 2023; revised 22 August 2023 and 27 October 2023; accepted 13 December 2023. Date of publication 8 January 2024; date of current version 24 January 2024. This work was supported by the National Geospatial-Intelligence Agency (NGA) University Research Initiative under Grant HM04762110005. *(Corresponding author: Chase Cañas.)*

The authors are with the Chester F. Carlson Center for Imaging Science, Rochester Institute of Technology, Rochester, NY 14623 USA (e-mail: cc1903@rit.edu).

Digital Object Identifier 10.1109/TGRS.2024.3351048

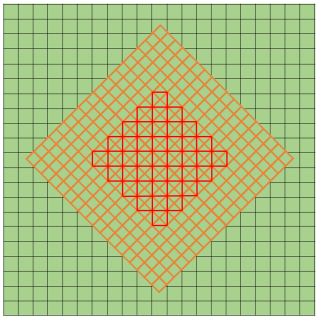

Fig. 2. Target fill fraction of pixel samples across the central region (red) of the lattice target (orange) when placed onto a background (green) is invariant to the pixel phasing or scan pattern of the remote sensor.

5) *Spatial Distortion:* Optical aberrations and misalignments distorts the signal traceability (e.g., keystone).
6) *Target Mask:* A ground truth target mask is manually created by a user and thus is susceptible to human error.

A. Advantages of the Lattice-Based Targets

The novel targets are a lattice-based structure that enables remote sensors to collect constant subpixel fractions of target material across large numbers of samples. The subpixel targets are invariant to the issues associated with traditional targets, which includes pixel phasing as shown in Fig. 2. This is unique, as historic datasets generally label subpixel targets but with random or unknown target fill fractions. The outcome for detection studies is an additional dimension to ROC curves, where the detection rate (P_D) is now a function of the false alarm rate (P_{FA}) and the target fill fraction (α), broadening research opportunities for algorithm comparison and system trade studies. Given large numbers of samples, confidence intervals are minimized in ROC curves [14], enabling more conclusive inferences on evaluations of detection. In addition to assessments of detection limits, the lattice-based targets enable an empirical validation of subpixel models which has been demonstrated using an early prototype of the design [15].

B. Overview

The design and demonstration of a novel target for hyperspectral subpixel detection is outlined, with an objective of collecting large numbers of subpixel samples with constant fill fractions. In Section II, the target design, system parameters, optics, and detector characteristics are discussed for achieving uniformity of target and background material across the optical and digital image. Methods for fabrication of the targets are presented in Section III, and details of the remote sensing field experiment for the targets are in Section IV. Validation of the target design objectives reside in Section V, and demonstration for a subpixel target detection scenario is in Section VI. To conclude, an empirical case study revealing impacts of a limited sample size on detection is outlined in Section VII, with limitations of the novel design discussed in Section VIII.

II. Design

The design of the novel target is a lattice structure consisting of repeating patterns of polygons (e.g., squares) with holes across 2-D. The target surface area is simply an area difference between inner and outer polygons, ($a_{\text{out}} - a_{\text{in}}$), and when normalized with a_{out} is the effective fill fraction α. A single parameter to characterize the effective fill fraction across the entire target is the inner wall width, w, of the structure, when given a constant pitch between central polygons. Illustrations are shown in Fig. 3. The polygons may be squares, hexagons, triangles, or any other geometric variation.

A. System Requirements

The subpixel target is geometrically characterized by three parameters, which include the overall area A, inner wall width w, and lattice pitch p_ℓ (distance between center polygon holes). This is illustrated in Fig. 4 for a hexagonal target, where the overall length L replaces the overall area A, for simplicity. The sensor parameters include the GSD and ground sample size (GSS), which co-vary as defined by the Q value of the sensor [16]. Appropriate combinations of these system parameters are required for the collection of large numbers of samples with constant fill fractions.

To achieve the design objectives, general guidelines include $p_\ell \leq \text{GSD}$ and $L \gg \text{GSD}$; further details will be outlined in the succeeding subsection. This ensures the collection of a large number of samples with constant fill fractions across the central region of the target. Samples across the edges of the target will not comprise of constant fill fractions, given the PSF of the sensor blurs the background material onto the target space. Furthermore, the remote sensor is required to fly at near-nadir conditions to minimize the error associated with the projected area of the lattice. This is attributed to a physical target having 3-D thickness, albeit the overall geometry is 2-D flat.

B. Optical Blur

The PSF of an optical system is a primary source of image degradation, apart from optical aberrations and misalignments. The PSF spreads radiant energy from a point object into the surrounding medium, effectively blurring the output image. The convolution equation is

$$g(x, y) = f(x, y) * h(x, y) + n(x, y) \tag{1}$$

where $g(x, y)$ is the image, $f(x, y)$ is the object, $h(x, y)$ is the PSF, and $n(x, y)$ is additive noise. Considering a remote sensor, the system PSF is the convolution of the PSF for each component

$$h_{\text{sys}} = h_{\text{opt}} * h_{\text{mot}} * h_{\text{det}} * h_{\text{elec}} * h_{\text{atm}} \tag{2}$$

where h_{opt} is the PSF of the optics, h_{mot} is the PSF of the platform motion, h_{det} is the PSF of the detector, h_{elec} is the PSF of the electronics, and h_{atm} is the PSF of the atmosphere. For a traditional target, the blur of the PSF increases uncertainty in the fill fraction of a pixel.

The effects of the PSF uniquely enhance the objectives of the lattice target, given a more uniform distribution of target material is established in the blurred image of the lattice. In general, the amount of blur can be characterized by the full-width at half-maximum (FWHM) of the PSF;

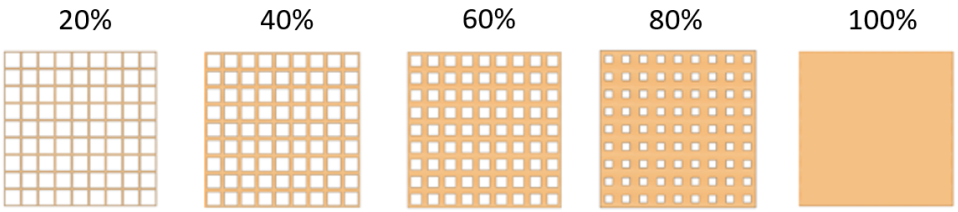

Fig. 3. Illustration of subpixel target design for varying nominal fill percentages.

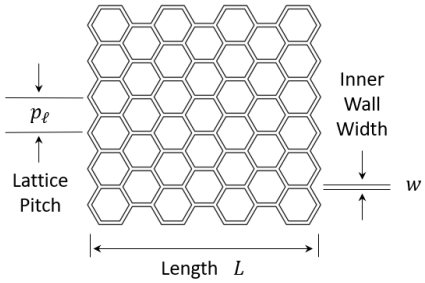

Fig. 4. Target design parameters for the lattice subpixel target.

when projected onto the ground is referred to as the GSS [17]. Uniformity of target material across the image plane of the sensor can then be characterized by a ratio of the GSS to lattice pitch (p_ℓ)

$$\Gamma = \frac{\text{GSS}}{p_\ell} \tag{3}$$

where increasing Γ increases target uniformity. To demonstrate these optical effects across a lattice-based target, a simulation was established considering a value of $\Gamma = 2$. A similar value was proposed for early experimentation with the subpixel targets in an empirical dataset [15]. The simulation involves the generation of a binary array (e.g., hexagonal lattice) convolved with a normalized Gaussian (i.e., generalized system PSF). The hexagonal geometry was selected given the radial symmetry with the Gaussian PSF would theoretically maximize uniformity. A demonstration is shown in Fig. 5. As observed, the blurred image after convolution exhibits visual uniformity across the central target region. The nominal fill fraction of the example lattice is $\alpha = 0.2$, calculated using the discrete ratio of computational pixels within the outer and inner hexagons of the binary array. A cross-sectional plot of the optically blurred image is shown in Fig. 6. Uniformity diminishes across the edges of the blurred lattice, as the PSF smears target material into the surrounding background. This simulates the optical effects in a real scenario.

To demonstrate the impacts of the Γ value on target uniformity across the image plane, a case study is shown in Fig. 7, which considers the equivalent target geometry ($\alpha = 0.2$) shown in Fig. 5. The results infer visual uniformity when $\Gamma \geq 1$. The simulation does assume a Gaussian PSF as a general baseline, although the actual shape certainly varies across different sensors, pixels, and flight lines. Regardless, the mechanism of blurring the lattice target to improve fill fraction uniformity across pixels remains consistent.

After the blurred image is cast onto the focal plane, detector sampling partitions radiant energy into discrete pixels. This process, along with optical blurring, improves the collection of constant fill fractions, given subpixels variations are effectively averaged when a pixel is integrated during detector sampling.

C. Detector Sampling

Detector sampling occurs after the target object is blurred onto the image plane of the sensor. While the GSS describes optical blur, the GSD describes how pixels are sampled across the detectors. The relationship between GSD and GSS is given by the Q value (GSS/GSD), which is constant for a given sensor with typical values ranging between 1 and 2. Increasing the size of the GSD, relative to a constant GSS, decreases the Q value and pixel-to-pixel variability of the target fill fraction. To investigate the Γ values required to achieve sufficient uniformity for a desired maximum pixel-to-pixel variability (e.g., 1%), a trade study was conducted simulating optical blur and detector sampling for a range of α, Γ, and Q values.

First, a series of unique lattice arrays were generated computationally for fill fractions, α, between $[0.1, 0.9]$ with a step size of 0.1. Second, optical blur of the lattices was simulated using a Gaussian PSF for Γ values between $[0.1, 1.5]$ with a step size of 0.1. Third, detector sampling of the blurred lattices was simulated using Q values between $[0.5, 2]$ with a step size of 0.1. As a result, 2160 unique detector sampled images were generated. An example of the detector sampling method is shown in Fig. 8, for a blurred lattice with nominal fill fraction of $\alpha = 0.2$ and $\Gamma = 0.75$ identical to an example shown in Fig. 7. Detector samples were simulated by averaging computational values within bins of the array determined from the GSD, or Q value, of the given sensor. The sampled image in Fig. 8(b) illustrates pixel-to-pixel variability of the target fill fraction, relative to the nominal value.

A cross-sectional plot of the detector sampled image ($\alpha = 0.2, \Gamma = 0.75$) is shown in Fig. 9. Nonuniform regions are observed around the lattice edges, in addition to pixel-to-pixel variability within the central region of the lattice. An RMSE metric is used to measure pixel-to-pixel variability of the target fill fraction of ith detector samples relative to the nominal value

$$\sigma_{\text{RMSE}} = \sqrt{\frac{\sum(\alpha_i - \hat{\alpha})^2}{N}} \tag{4}$$

where $\hat{\alpha}$ is the nominal target fill fraction, α_i is the effective target fill fraction, and N is the total number of

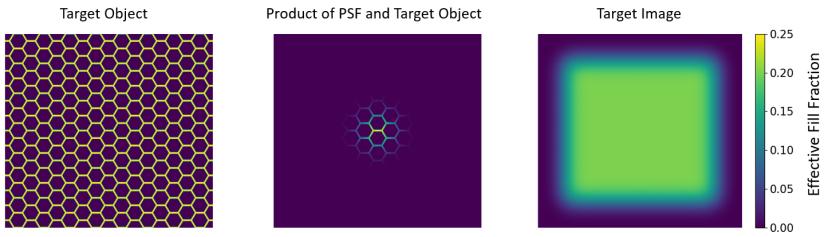

Fig. 5. Demonstration of the effects of a PSF across a lattice structure. The expected constant subpixel fraction of target material is $\alpha = 0.2$, with a GSS to lattice pitch ratio of $\Gamma = 2$.

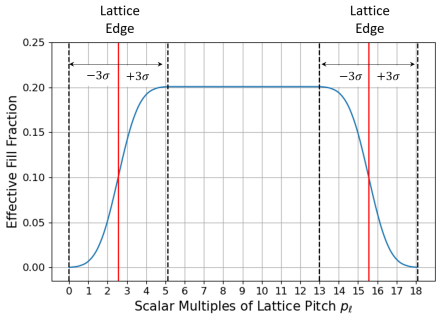

Fig. 6. Cross-sectional plot of the effective fill fraction of the blurred image for a lattice with $\alpha = 0.2$ and $\Gamma = 2$. Regions of nonuniformity reside within ± 3 standard deviations of the Gaussian PSF from the outer lattice edges.

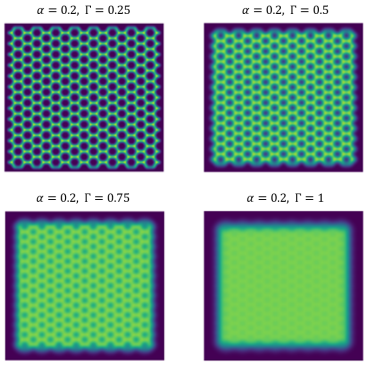

Fig. 7. Visual assessment of target uniformity for a lattice with a GSS to lattice pitch ratios $\Gamma = 0.25, 0.5, 0.75, 1$, and nominal target fill fraction $\alpha = 0.2$.

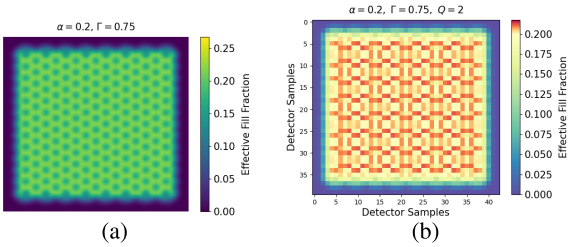

Fig. 8. Lattice target with nominal fill fraction $\alpha = 0.2$. (a) After optical blurring with $\Gamma = 0.75$. (b) After detector sampling with $\Gamma = 0.75$ and $Q = 2$.

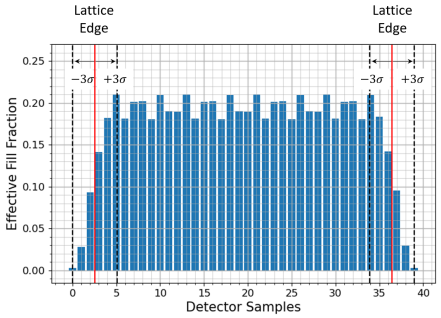

Fig. 9. Cross-sectional plot of the effective fill fraction of the detector sampled image for a lattice with $\alpha = 0.2$ and $\Gamma = 0.75$. Regions of pixel-to-pixel variability, reside within ± 3 standard deviations of a Gaussian PSF from the outer lattice edges; in addition, the central lattice region in this example.

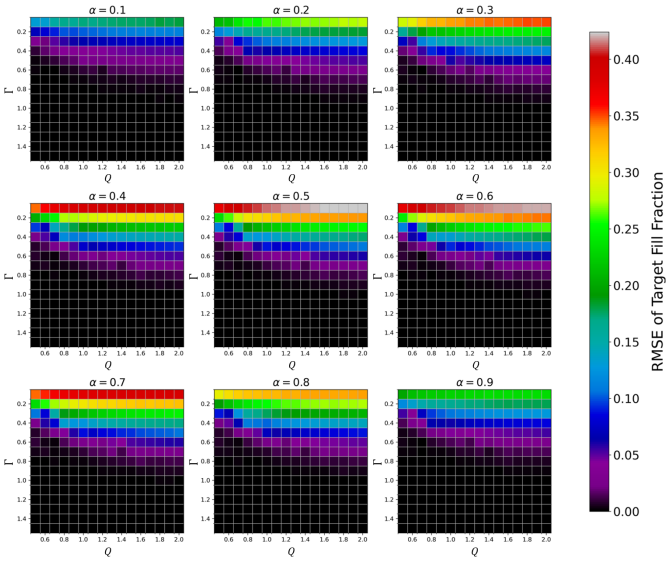

Fig. 10. Quantitative assessment of the RMSE of the target fill fraction as a function of three independent parameters (α, Γ, Q). The RMSE values denote pixel-to-pixel variability as a result of 2160 unique simulations for varying values of optical blur, $0.1 \leq \Gamma \leq 1.5$, detector sampling, $0.5 \leq Q \leq 2$, and hexagonal lattice structures with nominal fill fractions of $0.1 \leq \alpha \leq 0.9$.

detector samples. The RMSE equation is used for detector samples across the central region, excluding the outer region of ± 3 standard deviations of the PSF from the lattice edges. Given the range of α, Γ, and Q values considered, results for σ_{RMSE} across the 2160 simulations are shown in Fig. 10.

The results quantitatively confirm pixel-to-pixel variability of the target fill fraction, σ_{RMSE}, decreases for increasing values of Γ. In particular, it is observed sufficient uniformity of the blurred image occurs when $\Gamma > 0.8$ to achieve a $\sigma_{\text{RMSE}} < 1\%$ for all values of Q tested. This provides a general baseline for the lower limit of the Γ value needed to minimize error in the target fill fraction of subpixel samples. The results also quantitatively confirm σ_{RMSE} decreases for decreasing values of Q (i.e., increasing GSD). Furthermore, σ_{RMSE} appears to maximize when $\alpha = 0.5$, particularly for

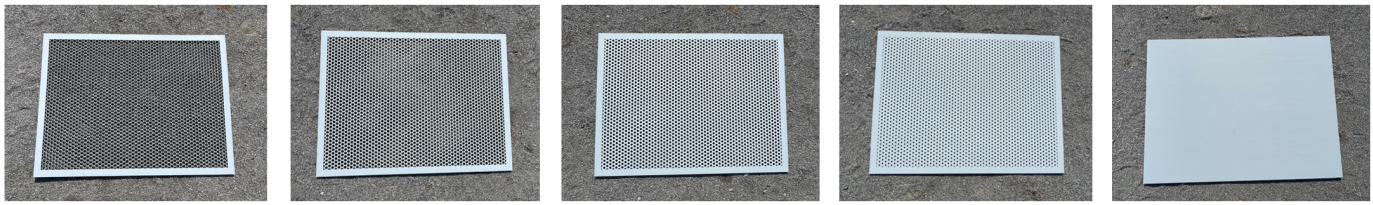

Fig. 11. Ground truth images of the subpixel targets ($\alpha = 0.2, 0.4, 0.6, 0.8, 1$) captured with a handheld camera.

large values of Q. Overall, the results provide a quantitative assessment of error associated with the retrieval of subpixel samples with constant fill fractions when a user is designing a data collection.

D. Review of Other Target Designs

Other novel target designs are featured in spectral unmixing datasets, using ground [18] and remote sensing [8], [19], [20] imagers. The design of the SHARE 2010 and 2012 targets developed by the Rochester Institute of Technology (RIT) consist of a checkerboard pattern of two materials. The proportions of squares between the two materials were modulated to enable constant area fractions of either 25%, 50%, or 75%, when sensed with the appropriate GSD. The limitations with this design occur when other area fractions are desired (i.e., other than in 25% increments). Furthermore, the SHARE targets were comprised of synthetic fabric squares adhered to a solid panel. This design does not allow mixed pixels to consist of natural backgrounds, which does incur in real target detection scenarios. The proposed lattice-based target design eliminates these shortcomings.

III. Fabrication

Initial prototypes of the subpixel targets were designed with CAD software; then fabricated using high density 1/8 in plywood and a CO_2 laser cutting apparatus. The small targets (approx. 12 × 12 in) were deployed into a basic data collection using an unmanned aerial system (UAS), as an initial technology demonstration. The mission was successful in retrieving small numbers (1–2 dozen) of near-constant fill fractions across each target, given the high spatial resolution of the sensor (GSD ≈ 4.5 cm) [15]. The initial prototypes consisted of square, triangular, and hexagonal geometries, with early analyses confirming the patterns were equally effective at generating samples with near-constant fill fractions. This was attributed to the large GSS to lattice pitch ratio ($\Gamma > 2$) established between the targets and aerial sensor. Nevertheless, important differences do exist between the geometries. Square and triangular lattices are rigid structures (with small bending moments), providing practical benefits during deployment of the delicate structures in the field. Hexagonal lattices are space efficient, enabling easier fabrication of very small fill fractions (e.g., 10%), while also likely providing more radial symmetry with the PSF to improve target uniformity. The optical advantages were prioritized, thus current versions of the subpixel targets use the hexagonal pattern.

Subsequent targets were fabricated to improve on the initial developments, with a focus on retrieval of large numbers of samples. Specifically, four lattice-based targets were fabricated with 1/4 in plywood and nominal fill fractions of 0.2, 0.4, 0.6, and 0.8; with a lattice pitch of $p_\ell = 2$ cm and overall dimensions of 45.3 × 33.7 in, as shown in Fig. 11. The overall dimensions were maximized given the limited bed size of the laser cutter was 48 × 36 in, and the increased thickness of the plywood (1/4 in) improved structural rigidity. When combined with the appropriate GSD (e.g., 4 cm), the retrieval of large numbers of samples ($n \approx$ 300–400) was predicted with constant fill fractions across each target. To minimize bi-directional reflectance (BRDF) effects, which induce inaccuracies in the retrieved fill fraction values, the targets were painted with a matte and speckled finish to approximate the properties of a diffuse reflector. This minimizes spectral variability which was observed in the initial investigation [15].

Extensive UAS resources are available in the Digital Imaging and Remote Sensing (DIRS) Laboratory at RIT [21], which accelerated the design, testing, and analysis process for the subpixel targets. In regards to fabrication, any homogeneous material is suitable for the targets; the choice of hardwood was appropriate for the laser cutter. Theoretically, the development of *any* nominal fill fraction is attainable given the appropriate material strength and design parameters of the target (w, p_ℓ).

IV. Field Experiment

A hyperspectral data collection occurred on September 9, 2022, at the Tait Preserve of RIT in Rochester, NY: a 177 acre estate, featuring diverse landscapes of open fields, hills, forests, and a 60 acre lake. The dataset was used for validation and demonstration of the subpixel targets. The altitude of the UAV during data collection was approximately 200 ft, with clear sky conditions. The UAV was flown at near-nadir ($\theta_z \approx 2.5°$–$3°$) conditions across the subpixel targets, per design requirement. A 270 band hyperspectral sensor (Headwall Nano-Hyperspec) in the VIS-NIR spectral range (0.4–1 μm) was mounted onto a DJI Matrice 600 UAV. The subpixel targets were deployed across a uniform gravel path, with ground truth images shown in Fig. 11. The scene consisted of a diverse range of background classes, including both man-made and natural materials, as shown in a flight line in Fig. 12. The data collection included a GSD ≈4 cm with a lattice pitch $p_\ell = 2$ cm. The Q value of the sensor is estimated between 1 and 1.5, through observation of PSF characteristics from an adjacent UAV case study using illuminated point sources [22]. Therefore, it is predicted an estimated Γ between 2 and 3 was established during the data collection. These system specifications, along with the large overall dimensions of the lattice targets (45.3 × 33.7 in) enabled

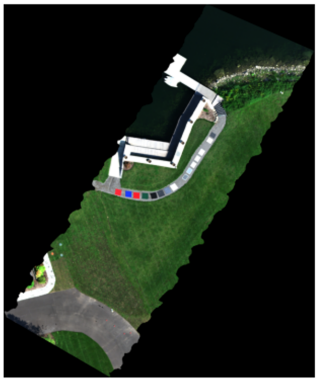

Fig. 12. RGB render of HSI data collected using a UAS across the Tait Preserve of RIT in Rochester, NY, USA.

the retrieval of a large number of samples with constant fill fractions. The optical simulation in Fig. 5 considered a similar Γ value as what was predicted in the data collection. Therefore, excellent uniformity of constant target fill fractions across pixels was expected from the real data.

V. Validation

The retrieval of image pixels with constant fill fractions across the lattice targets was validated using hyperspectral data from the field experiment in Fig. 12. Analysis of real data supports the proposal that fill fractions nominally calculated from the geometry of the lattices, are invariant to the effects of the remote sensing system (i.e., atmosphere, sensor, processing).

The method involves using spectral linear unmixing to compute abundance fractions of the target endmember across the image pixels of lattice. Then compared these abundances with the nominal values assigned to each target. The target endmember was defined by averaging approximately 200 image pixels across the central region of the 100%, or full-pixel, target. Boundary regions across the target were avoided, due to contamination of background material from the blurring of the PSF. No unit-sum constraint was applied, to allow any variability in the retrieved target abundance to be observed. Otherwise, the unit-sum constraint would likely propagate error associated with background spectral variability into the estimate of the target abundance. Furthermore, minimal spectral variability was observed associated with the target material (chemical and radiometric) and sensor noise, reducing error in the unmixing method. The average standard deviation across all bands of available full-pixel target samples ($n \approx 400$) within the image was 0.75% reflectance.

The validation results are shown in Fig. 13, which include histograms of the target abundance scores across the central regions of the lattice targets. A supporting set of validation images, in Fig. 14, include an RGB render of the HSI data above the lattice targets and a corresponding abundance colormap of the target endmember. This visually demonstrates the uniformity of samples with near-constant fill fractions. Furthermore, examination of the histograms demonstrates the retrieval of large numbers of samples ($n \approx 300$–400) retrieved across each subpixel target. The mean abundance percentages across each histogram (99.97, 80.24, 62.11, 41.27, 19.74) co-align with the nominal values with minimal percent differences (0.03, 0.24, 2.11, 1.27, 0.26). The standard deviation percentages (relative to the mean abundances) across each histogram are 1.18, 1.02, 1.19, 1.39, and 1.43 for the nominal 100%, 80%, 60%, 40%, and 20% targets, respectively.

Error in the subpixel abundance distributions is attributed to a variety of factors, with many uncorrelated to any developmental issues associated with the targets. For example, variability in the 100% target distribution shown in Fig. 13 is attributed to inherent chemical and micro-structure variations in the material itself and sensor noise in the imaging system. This source of error is propagated through all the other histograms, given the spectral unmixing method considers just a single reference spectra, or endmember. Additional possible sources of error include small BRDF effects across the targets, attributed to nonhorizontal target orientations relative to the ground. However, attempts to minimize BRDF effects were implemented before data collection, through careful deployment of the targets with a level measuring tool and application of multiple coats of matte paint during fabrication. In addition, it is predicted the sensor viewing angle ($\theta_z \approx 2.5°$–$3°$) from nadir may contribute approximately 1% error in the target fill fraction, determined analytically using geometry of the lattice structures (see Section VIII for further details).

VI. Target Detection Demonstration

To demonstrate the functionality of the lattice-based targets for subpixel target detection, an example scenario was established using HSI data collected as shown in Fig. 12. A ground truth mask was developed for five independent target classes, associated with pixels with constant fill fractions (0.2, 0.4, 0.6, 0.8, 1) within central regions ($n \approx 300$–400) of each subpixel target. Nonuniform subpixels across outer edges of the targets were masked with conservative guard regions (null), to decouple the analysis from subpixel targets with unknown fill fractions. Background pixels were defined across all remaining pixels within the flight line.

The target reference spectrum for the detector algorithm was selected using the mean of approximately 400 image samples across the central region of the 100% target. Although many algorithms exist for subpixel detection, two were selected for demonstration purposes which include the matched filter (MF) and adaptive cosine estimator (ACE)

$$w_{\mathrm{MF}}(\mathbf{x}) = \frac{(\mathbf{t}-\boldsymbol{\mu}_b)^T \boldsymbol{\Sigma}_b^{-1}(\mathbf{x}-\boldsymbol{\mu}_b)}{(\mathbf{t}-\boldsymbol{\mu}_b)^T \boldsymbol{\Sigma}_b^{-1}(\mathbf{t}-\boldsymbol{\mu}_b)} \tag{5}$$

$$w_{\mathrm{ACE}}(\mathbf{x}) = \frac{\left[(\mathbf{t}-\boldsymbol{\mu}_b)^T \boldsymbol{\Sigma}_b^{-1}(\mathbf{x}-\boldsymbol{\mu}_b)\right]^2}{(\mathbf{t}-\boldsymbol{\mu}_b)^T \boldsymbol{\Sigma}_b^{-1}(\mathbf{t}-\boldsymbol{\mu}_b)(\mathbf{x}-\boldsymbol{\mu}_b)^T \boldsymbol{\Sigma}_b^{-1}(\mathbf{x}-\boldsymbol{\mu}_b)} \tag{6}$$

where $\mathbf{x}$ is an image pixel, $\boldsymbol{\mu}_b$ and $\boldsymbol{\Sigma}_b^{-1}$ are the mean vector and inverse covariance matrix of the background, and $\mathbf{t}$ is the target reference vector.

Preexisting subpixel datasets provide target samples with unknown fill fractions, α, and the unknown corresponding number of samples, N_α. To demonstrate the results of a typical detection performance evaluation, probabilities of detection (P_D) and false alarm (P_{FA}) were computed for

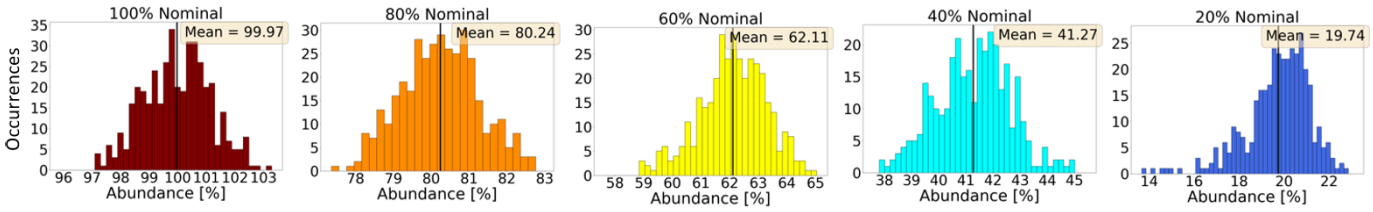

Fig. 13. Abundance histograms of the target endmember from samples across central regions of each subpixel target.

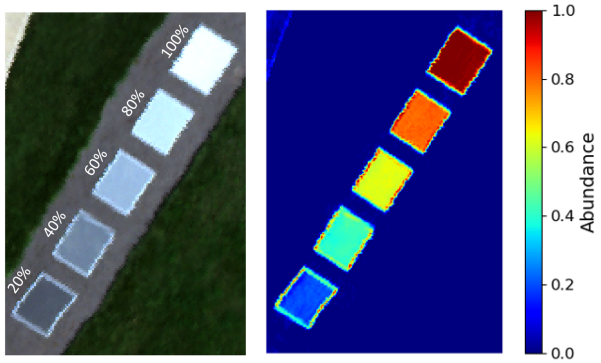

(a) (b)

Fig. 14. (a) Nominal target percentages of subpixel targets and (b) corresponding abundance map of target endmember.

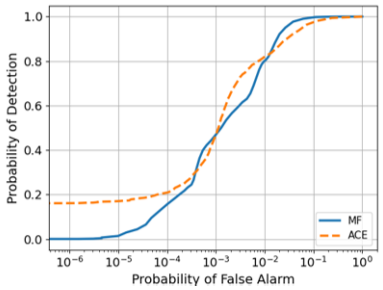

Fig. 15. Performance comparison of target detection algorithms (MF and ACE) when considering approximately 1800 subpixel samples with fill fractions of 0.2, 0.4, 0.6, 0.8, and 1.

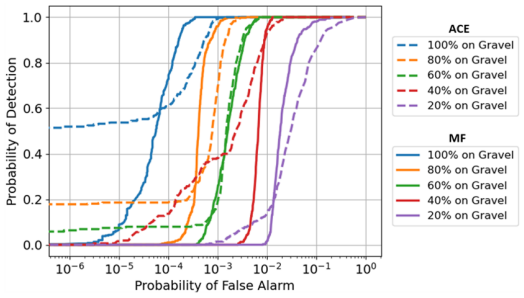

Fig. 16. Performance comparison of target detection algorithms (MF and ACE) when considering partitioned groups of constant subpixel fill fractions of 0.2, 0.4, 0.6, 0.8, and 1.

algorithm output score distributions *without* knowledge of the target fill fraction across the available 1800 approximate subpixel samples. The results are shown with ROC curves in Fig. 15, using the MF and ACE algorithms.

To demonstrate the value of the lattice-based targets, probabilities of detection (P_D) and false alarm (P_{FA}) were also computed for algorithm output score distributions *with* knowledge of the target fill fraction across partitioned sample groups of constant fractions. The ROC curves for each subpixel target group (0.2, 0.4, 0.6, 0.8, 1) are shown in Fig. 16, using the MF and ACE algorithms. The results infer more definitive conclusions on algorithm performance given the specific background scenario. When comparing the MF and ACE algorithms, it is observed performance is comparable *without* knowledge of the target fill fraction. However, *with* knowledge, performance can now be assessed as a function of the fill fraction α at various false alarms of interest P_{FA}.

VII. Impacts of Sample Size on Detection

In historical datasets for subpixel target detection, a limited number of target samples are available for experimentation. Therefore, performance results are subject to variability if the experiment were repeated with an alternate number of random samples derived from a larger population. To quantify this uncertainty, confidence intervals or regions in ROC curves have been developed [14]. The design of the lattice-based target mitigates this issue, given the retrieval of a large number of samples (e.g., 300–400). To demonstrate the impacts of sample size on detection, a case study for random sampling limited numbers of mixed target spectra was performed.

A limited sample size of 5, 10, 50, and 100 target subpixels was considered for each fill fraction of 0.2, 0.4, 0.6, 0.8, and 1. For each limited sample size (5, 10, 50, 100), an ensemble of 50 groups (randomly sampled with replacement) was collected from a larger distribution of available samples ($n \approx 300$–400). The choice of 50 groups was selected given it was assumed 50 random iterations would sufficiently demonstrate variability in the ROC curves. The results of the limited sample trade study, using the identical algorithm and background statistics outlined in Section VI, are shown in Fig. 17,

The results demonstrate significant variability occurs in ROC curves when a small number of random target samples (e.g., 5, 10) are considered from a larger population. The shaded regions in Fig. 17 represent the envelope of minimum and maximum P_D values across the 50 random iterations. This reiterates the importance of confidence intervals or regions when reporting ROC curves with a small number of target samples. The variability of the ROC curves decreases significantly when the number of target samples $n \geq 50$. When $n \geq 100$, the variability in ROC curves, across the P_D direction, becomes marginal. This validates the efficacy of the lattice targets implemented in the UAS dataset for generating 300–400 samples of constant fill fractions per target.

VIII. Limitations of Lattice-Based Targets

The lattice target design was proven effective for the collection of constant fill fractions of large numbers of samples with

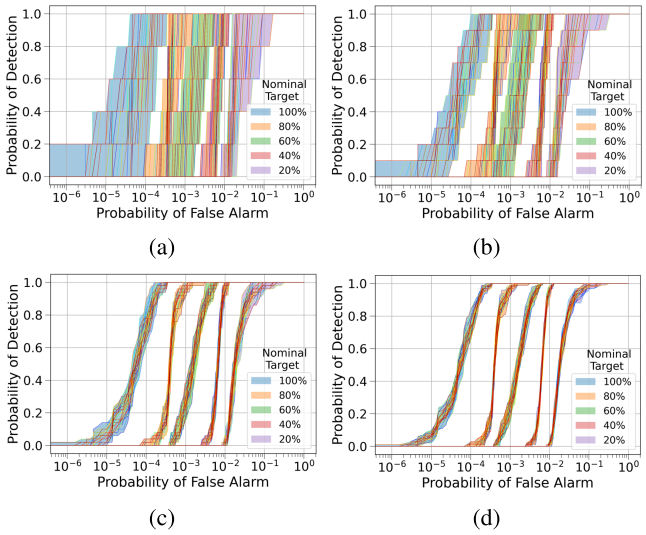

Fig. 17. ROC curves using 50 random groups of (a) five samples, (b) ten samples, (c) 50 samples, and (d) 100 samples with constant subpixel target percentages from the MF.

the appropriate system parameters; however, limitations do exist. The fabrication method (laser cutter) constrains targets to sizes smaller than the spatial resolution of airborne or spaceborne sensors. Therefore, additional efforts are required to plan larger-scale experiments with sensors at higher altitudes. Although the optical depth of the atmosphere varies between UAS, airborne, and spaceborne systems, it is assumed inferences derived from UAS data extend to alternate platforms.

Other limitations include deviations of the target fill fraction for off-nadir sensor viewing angles, θ_v. An analytical equation, derived in the Appendix, for the off-nadir fill fraction is

$$\alpha_\theta = \alpha_n + \tau\sqrt{1-\alpha_n}\cdot\tan\theta_v \tag{7}$$

where $\tau = h/p_\ell$ denotes the lattice thickness (or height) to lattice pitch ratio, for a unit-less expression. The equation assumes the material of the lattice inner wall is equivalent to the upper surface. Deviations of the target fill fraction, α_θ, relative to the nominal values for a range of viewing angles and τ ratios are shown in Fig. 18. In the field experiment, $\tau = 0.3175$ characterizes the target geometry. Therefore, a 1% error in target fill fraction is estimated when the viewing angle is approximately 2.5°–3° off-nadir, using (7). Additional error in the target fill fraction is associated with the target tilt relative to the ground not being perfectly flat, which is coupled to the error associated with off-nadir sensor viewing angles.

A "self shadowing" effect within a lattice target occurs when the lattice pitch is small (e.g., 2 cm) relative to the target's 3-D thickness (e.g., 1/4 in). An analytical equation, derived in the Appendix, for the fraction of shaded background within a mixed pixel is

$$\beta = \tau\cdot\frac{\tan\theta_s}{\sqrt{1-\alpha_n}} \tag{8}$$

where θ_s is the solar zenith angle and $\tau = h/p_\ell$ creates a unit-less expression. The results across a range of solar zenith angles and τ ratios are shown in Fig. 19. The self-shadow effect, although can be interpreted as a limitation,

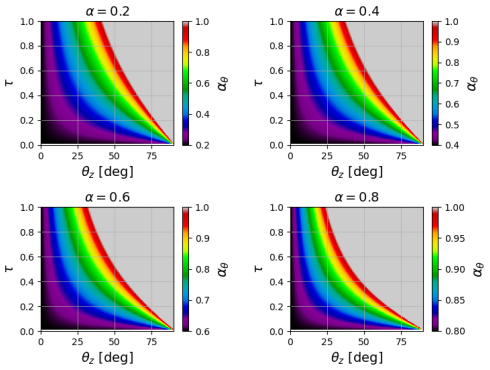

Fig. 18. Assessment of the target fill fraction (α_θ) relative to the nominal value (α) as a function of off-nadir sensor viewing angle (θ_z) and lattice thickness to pitch ratio (τ).

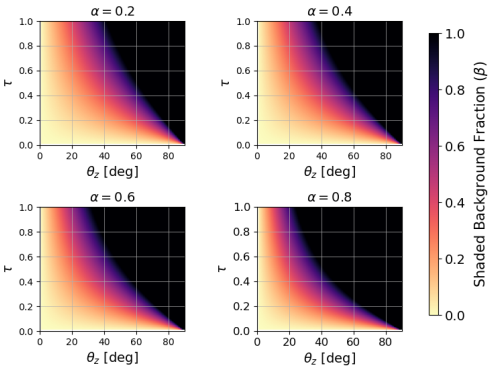

Fig. 19. Assessment of the shaded background fraction (β) as function of the solar zenith angle (θ_z) and lattice thickness to pitch ratio (τ), for varying nominal fill fraction targets (α).

has also enabled new research on impacts of fully illuminated subpixel targets on partially shaded subpixel backgrounds [23]. Regardless of the lattice target impinging a shadow onto the background, the target material remains fully illuminated with image pixels consisting of constant subpixel fill fractions.

Lastly, if the lattice-based targets are placed onto a single background, the diversity of subpixel samples mixed with different backgrounds is limited. However, the availability of large numbers of subpixels samples of targets over a single background provides conclusive results of detection for the given target-background combination and surrounding scene.

IX. Conclusion

A lattice-based target design for subpixel detection experiments was proposed for expanding research capabilities in the field. The design enables a hyperspectral remote sensor to collect large numbers of samples with constant fill fractions, α, for a desired target material, given the appropriate target design (w, L, p_ℓ) and sensor (Q) parameters of the system. A unique characteristic of the targets involve the sensor PSF enhancing uniformity of target material across the image. A metric to characterize this uniformity was defined as the GSS to lattice pitch ratio, or Γ. A trade study assessing pixel-to-pixel variability after detector sampling, σ_{RMSE}, as function of α, Γ and Q was performed. Subpixel targets for a range of fill fractions (0.2, 0.4, 0.6, 0.8) were fabricated

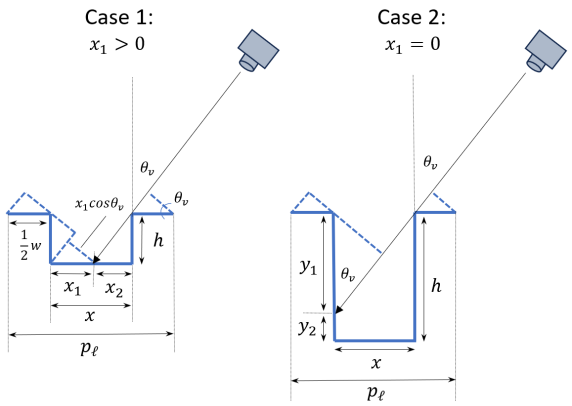

Fig. 20. Illustration of a cross-sectional square lattice pattern for varying combinations of lattice height to pitch ratios $\tau = h/p_\ell$ and sensor viewing angles θ_v.

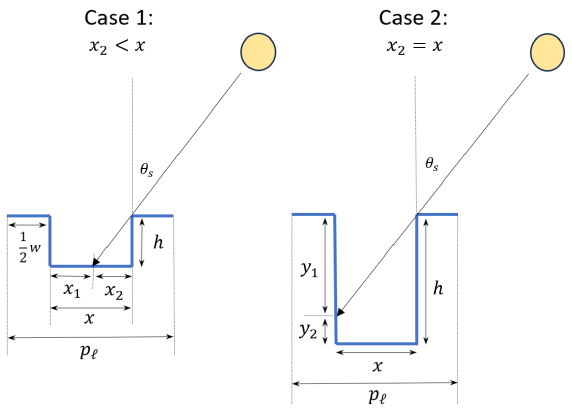

Fig. 21. Illustration of a cross-sectional square lattice pattern for varying combinations of lattice height to pitch ratios $\tau = h/p_\ell$ and solar angles θ_s.

and deployed into a UAS data collection, producing 300–400 uniform samples per target. Nominal fill fractions were validated using spectral unmixing to compute target abundance fractions of the mixed pixels. A scenario for subpixel target detection was then established for demonstrating functionality of the targets, using independent ROC curves computed from groups of samples with constant fill fractions. The detection impacts when given a limited number of target samples were demonstrated empirically when considering ensembles (50) of identical scenarios (i.e., background statistics) for varying fill fraction groups of nonidentical numbers of target samples (e.g., 5, 10, 50, 100). The results imply the availability of large numbers of samples (e.g., 300–400) collected across the lattice targets provide definitive conclusions on detection evaluations (e.g., algorithm comparison) for a specific scene and combination of subpixel target-background material.

APPENDIX

There are two cases for deriving the fill fraction for off-nadir sensor viewing angles (zenith), as observed in Fig. 20. For a generalized assessment, both cases assume a square patterned lattice with an azimuth viewing angle perpendicular to the lattice edge.

For case 1, the target fill fraction observed for off-nadir sensor viewing angles, α_θ, is a ratio of projected areas within a segment of the repeating lattice pattern

$$\alpha_\theta = \frac{A_{t,P}}{A_{t,P} + A_{b,P}} = \frac{p_\ell^2 \cos\theta_v - x x_1 \cos\theta_v}{p_\ell^2 \cos\theta_v} = 1 - \frac{x x_1}{p_\ell^2}. \quad (9)$$

where θ_v is the sensor viewing angle, p_ℓ^2 is the total area across a lattice segment, and $x x_1$ is the rectangular area visible from the sensor. The equation assumes the inner wall material of the lattice target is equivalent to the upper surface. The $x x_1$ term can be expanded

$$x x_1 = x(x - x_2) = x^2 - x \cdot h \tan\theta_v \quad (10)$$

with $x = p_\ell \sqrt{1 - \alpha_n}$ derived from the nominal target fill fraction for nadir sensor viewing angles

$$\alpha_n = \frac{A_t}{A_t + A_b} = \frac{p_\ell^2 - x^2}{p_\ell^2}. \quad (11)$$

Therefore, the expression

$$x x_1 = p_\ell^2 (1 - \alpha_n) - p_\ell \sqrt{1 - \alpha_n} \cdot h \tan\theta_v \quad (12)$$

is now in terms of parameters $(p_\ell, \alpha_n, \theta_v)$. Substituting (12) into (9), the target fill fraction for off-nadir sensor viewing angles after simplification is

$$\alpha_\theta = \alpha_n + \frac{h}{p_\ell} \sqrt{1 - \alpha_n} \cdot \tan\theta_v. \quad (13)$$

Considering $\tau = h/p_\ell$, the lattice thickness (or height) to lattice pitch ratio, α_θ is now a unit-less expression

$$\alpha_\theta = \alpha_n + \tau \sqrt{1 - \alpha_n} \cdot \tan\theta_v. \quad (14)$$

For case 2, the background material is nonobservable from the sensor ($\alpha_\theta = 1$). This occurs when the viewing angle

$$\theta_v > \arctan\left(\frac{x}{h}\right) \quad (15)$$

$$\theta_v > \arctan\left(\frac{\sqrt{1 - \alpha_n}}{\tau}\right). \quad (16)$$

Similarly, there are two cases for deriving the shaded background fraction due to varying solar angles, as observed in Fig. 21. For a generalized assessment, both cases again assume a square patterned lattice with an azimuth viewing angle perpendicular to the lattice edge.

For case 1, the fraction of the shaded background is

$$\beta = \frac{x_2}{x} = \frac{h \cdot \tan\theta_s}{p_\ell \sqrt{1 - \alpha_n}} \quad (17)$$

$$\beta = \tau \cdot \frac{\tan\theta_s}{\sqrt{1 - \alpha_n}} \quad (18)$$

where θ_s is the solar zenith angle and $\tau = h/p_\ell$ is substituted for a unit-less expression. For case 2, the background is entirely shaded ($\beta = 1$) which occurs, similar to (16), when the solar zenith angle

$$\theta_s > \arctan\left(\frac{\sqrt{1 - \alpha_n}}{\tau}\right). \quad (19)$$

ACKNOWLEDGMENT

The authors would like to thank Nina Raqueno and Tim Bauch, research staff at the Digital Imaging and Remote Sensing Laboratory, for leading operations in the unmanned aerial system (UAS) data collection. They acknowledge Dr. Emmett Ientilucci and Colin Maloney for their assistance with planning of the hyperspectral data collection. They also thank Micah Ross for his assistance collecting ground truth spectral measurements.

REFERENCES

[1] D. Manolakis and G. Shaw, "Detection algorithms for hyperspectral imaging applications," *IEEE Signal Process. Mag.*, vol. 19, no. 1, pp. 29–43, Jan. 2002, doi: 10.1109/79.974724.

[2] H. Kwon and N. M. Nasrabadi, "A comparative analysis of kernel subspace target detectors for hyperspectral imagery," *EURASIP J. Adv. Signal Process.*, vol. 2007, no. 1, Dec. 2006, Art. no. 029250, doi: 10.1155/2007/29250.

[3] X. Jin, S. Paswaters, and H. Cline, "A comparative study of target detection algorithms for hyperspectral imagery," *Proc. SPIE*, vol. 7334, pp. 682–693, Apr. 2009, doi: 10.1117/12.818790.

[4] N. M. Nasrabadi, "Hyperspectral target detection : An overview of current and future challenges," *IEEE Signal Process. Mag.*, vol. 31, no. 1, pp. 34–44, Jan. 2014, doi: 10.1109/MSP.2013.2278992.

[5] D. Snyder, J. Kerekes, I. Fairweather, R. Crabtree, J. Shive, and S. Hager, "Development of a web-based application to evaluate target finding algorithms," in *Proc. IEEE Int. Geosci. Remote Sens. Symp.*, vol. 2, Jul. 2008, pp. 915–918, doi: 10.1109/IGARSS.2008.4779144.

[6] D. Manolakis, "Is there a best hyperspectral detection algorithm?" *Proc. SPIE*, vol. 7334, pp. 13–28, Apr. 2009, doi: 10.1117/2.1200906.1560.

[7] R. C. Olsen et al., "Target detection in a forest environment using spectral imagery," *Proc. SPIE*, 1997. [Online]. Available: https://www.spiedigitallibrary.org/conference-proceedings-of-spie/3118/0000/Target-detection-in-a-forest-environment-using-spectral-imagery/10.1117/12.283842.short#_=_

[8] J. P. Kerekes, K. Ludgate, A. Giannandrea, N. G. Raqueno, and D. S. Goldberg, "SHARE 2012: Subpixel detection and unmixing experiments," *Proc. SPIE*, vol. 8743, May 2013, Art. no. 87430H, doi: 10.1117/12.2016274.

[9] P. Gader, A. Zare, R. Close, J. Aitken, and G. Tuell, "MUUFL gulfport hyperspectral and LiDAR airborne data set," Dept. Comput. Inf. Sci. Eng., Univ. Florida, Gainesville, FL, USA, Tech. Rep., 2013-570, Oct. 2013. [Online]. Available: https://github.com/GatorSense/MUUFLGulfport

[10] N. Acito, S. Matteoli, A. Rossi, M. Diani, and G. Corsini, "Hyperspectral airborne 'viareggio 2013 trial' data collection for detection algorithm assessment," *IEEE J. Sel. Topics Appl. Earth Observ. Remote Sens.*, vol. 9, no. 6, pp. 2365–2376, Jun. 2016, doi: 10.1109/JSTARS.2016.2531747.

[11] E. J. Ientilucci, "New SHARE 2010 HSI-LiDAR dataset: Re-calibration, detection assessment and delivery," *Proc. SPIE*, vol. 9976, pp. 121–129, Sep. 2016, doi: 10.1117/12.2239044.

[12] S. S. Jha and R. R. Nidamanuri, "Gudalur spectral target detection (GST-D): A new benchmark dataset and engineered material target detection in multi-platform remote sensing data," *Remote Sens.*, vol. 12, no. 13, p. 2145, Jul. 2020, doi: 10.3390/rs12132145.

[13] Y. Cohen, Y. August, D. G. Blumberg, and S. R. Rotman, "Evaluating subpixel target detection algorithms in hyperspectral imagery," *J. Electr. Comput. Eng.*, vol. 2012, pp. 1–15, Jan. 2012, doi: 10.1155/2012/103286.

[14] J. Kerekes, "Receiver operating characteristic curve confidence intervals and regions," *IEEE Geosci. Remote Sens. Lett.*, vol. 5, no. 2, pp. 251–255, Apr. 2008, doi: 10.1109/LGRS.2008.915928.

[15] C. Cañas, J. P. Kerekes, E. J. Ientilucci, and S. D. Brown, "Empirical validation of a hyperspectral systems model for subpixel target detection using data from a new UAS field collection," *Proc. SPIE*, vol. 12235, pp. 98–103, Sep. 2022, doi: 10.1117/12.2633609.

[16] R. D. Fiete, "Image quality and [lambda] FN/p for remote sensing systems," *Opt. Eng.*, vol. 38, no. 7, pp. 1229–1240, Jul. 1999, doi: 10.1117/1.602169.

[17] J. R. Schott, *emote Sensing: The Image Chain Approach*. Oxford, U.K.: Oxford Univ. Press, May 2007.

[18] C. V. S. S. Manohar Kumar, S. S. Jha, R. R. Nidamanuri, and V. K. Dadhwal, "Multi-resolution terrestrial hyperspectral dataset for spectral unmixing problems," *Data Brief*, vol. 43, Aug. 2022, Art. no. 108331, doi: 10.1016/j.dib.2022.108331.

[19] J. A. Herweg et al., "Spectir hyperspectral airborne Rochester experiment data collection campaign," *Proc. SPIE*, vol. 8390, pp. 717–726, May 2012, doi: 10.1117/12.919268.

[20] D. S. Goldberg, J. P. Kerekes, and K. A. Canham, "Hyperspectral linear unmixing: Quantitative evaluation of novel target design and edge unmixing technique," in *Proc. Western New York Image Process. Workshop*, Nov. 2012, pp. 25–28, doi: 10.1109/WNYIPW.2012.6466651.

[21] D. S. Kaputa, T. Bauch, C. Roberts, D. McKeown, M. Foote, and C. Salvaggio, "Mx-1: A new multi-modal remote sensing UAS payload with high accuracy GPS and IMU," in *Proc. IEEE Syst. Technol. Remote Sensing Appl. Through Unmanned Aerial Syst.*, Feb. 2019, pp. 1–4, doi: 10.1109/STRATUS.2019.8713292.

[22] D. Conran and E. J. Ientilucci, "Interrogating UAV image and data quality using convex mirrors," in *Proc. IEEE Int. Geosci. Remote Sens. Symp.*, Jul. 2022, pp. 4525–4528.

[23] C. Canas, J. Kerekes, C. Maloney, E. Ientilucci, and S. Brown, "Impacts of fully illuminated targets on partially shaded backgrounds for a multiclass subpixel target detection scenario," in *Proc. IEEE Int. Geosci. Remote Sensing Symp.*, Jul. 2023, pp. 2266–2269.

[24] J. P. Kerekes and J. E. Baum, "Spectral imaging system analytical model for subpixel object detection," *IEEE Trans. Geosci. Remote Sens.*, vol. 40, no. 5, pp. 1088–1101, May 2002, doi: 10.1109/TGRS.2002.1010896.

Chase Cañas (Graduate Student Member, IEEE) received the B.S. degree in physics from the University of California at Santa Barbara, Santa Barbara, CA, USA, in 2015, and the M.S. degree in physics from California State University, Long Beach, CA, USA, in 2020. He is currently pursuing the Ph.D. degree with the Chester F. Carlson Center for Imaging Science, Rochester Institute of Technology, Rochester, NY, USA.

He was employed at the NASA Jet Propulsion Laboratory, Pasadena, CA, USA, as an Engineering Graduate Student from June 2019 to August 2020, where he assisted in radiometric calibration and system engineering for hyperspectral atmospheric sounders (e.g., AIRS). His research interests include modeling of remote sensing systems, sensor calibration, and instrument design.

John P. Kerekes (Senior Member, IEEE) received the B.S., M.S., and Ph.D. degrees in electrical engineering from Purdue University, West Lafayette, IN, USA, in 1983, 1986, and 1989, respectively.

From 1983 to 1984, he was a Member of the Technical Staff with the Space and Communications Group, Hughes Aircraft Company, El Segundo, CA, USA, where he performed circuit design for communications satellites. From 1986 to 1989, he was a Graduate Research Assistant with the School of Electrical Engineering and the Laboratory for Applications of Remote Sensing, Purdue University. From 1989 to 2004, he was a Technical Staff Member with the Lincoln Laboratory, Massachusetts Institute of Technology, Lexington, MA, USA. Since 2004, he has been with the Chester F. Carlson Center for Imaging Science, Rochester Institute of Technology, Rochester, NY, USA, where he is currently a Research Professor. His research interests include the modeling and analysis of remote sensing system performance in pattern recognition and geophysical parameter retrieval applications.

Dr. Kerekes is a member of Tau Beta Pi, Eta Kappa Nu, the American Geophysical Union, and the American Society for Photogrammetry and Remote Sensing. He is a Senior Member of SPIE. From 1995 to 2004, he served as the Founding Chair for the Boston Section Chapter, IEEE Geoscience and Remote Sensing Society (GRSS). From 2007 to 2010, he served as the Founding Chair for the Western New York Chapter, IEEE GRSS. He was the Co-General Chair of IGARSS 2008 held in Boston, MA, USA. From 2010 to 2015, he served on the GRSS Administrative Committee (AdCom). In 2017, he received the GRSS Outstanding Service Award. He is currently serving as the GRSS Chief Financial Officer.